

## HYDROGEN DIMERS IN GIANT-PLANET INFRARED SPECTRA

LEIGH N. FLETCHER,<sup>1</sup> MAGNUS GUSTAFSSON,<sup>2</sup> AND GLENN S. ORTON<sup>3</sup>

<sup>1</sup>*Department of Physics and Astronomy, University of Leicester, University Road, Leicester, LE1 7RH, UK.*

<sup>2</sup>*Applied Physics, Division of Materials Science, Department of Engineering Science and Mathematics, Luleå University of Technology, SE-97187 Luleå, Sweden*

<sup>3</sup>*Jet Propulsion Laboratory, California Institute of Technology, 4800 Oak Grove Drive, Pasadena, CA 91109, USA*

(Accepted December 11, 2017)

Submitted to ApJ Supplement

### ABSTRACT

Despite being one of the weakest dimers in nature, low-spectral-resolution Voyager/IRIS observations revealed the presence of (H<sub>2</sub>)<sub>2</sub> dimers on Jupiter and Saturn in the 1980s. However, the collision-induced H<sub>2</sub>-H<sub>2</sub> opacity databases widely used in planetary science (Borysow et al. 1985; Orton et al. 2007; Richard et al. 2012) have thus far only included free-to-free transitions and have neglected the contributions of dimers. Dimer spectra have both fine-scale structure near the S(0) and S(1) quadrupole lines (354 and 587 cm<sup>-1</sup>, respectively), and broad continuum absorption contributions up to ±50 cm<sup>-1</sup> from the line centres. We develop a new *ab initio* model for the free-to-bound, bound-to-free and bound-to-bound transitions of the hydrogen dimer for a range of temperatures (40-400 K) and para-hydrogen fractions (0.25-1.0). The model is validated against low-temperature laboratory experiments, and used to simulate the spectra of the giant planets. The new collision-induced opacity database permits high-resolution (0.5-1.0 cm<sup>-1</sup>) spectral modelling of dimer spectra near S(0) and S(1) in both Cassini Composite Infrared Spectrometer (CIRS) observations of Jupiter and Saturn, and in Spitzer Infrared Spectrometer (IRS) observations of Uranus and Neptune for the first time. Furthermore, the model reproduces the dimer signatures observed in Voyager/IRIS data near S(0) (McKellar 1984) on Jupiter and Saturn, and generally lowers the amount of para-H<sub>2</sub> (and the extent of disequilibrium) required to reproduce IRIS observations.

*Keywords:* atmospheres, spectroscopy

arXiv:1712.02813v1 [astro-ph.EP] 7 Dec 2017

## 1. INTRODUCTION

Far-infrared spectra of giant planet atmospheres are dominated by continuum absorption resulting from collisions between molecular hydrogen and helium. This  $\text{H}_2\text{-H}_2$  and  $\text{H}_2\text{-He}$  collision-induced absorption (CIA) provides a thermometer to measure the thermal structure of the upper tropospheres of Jupiter, Saturn, Uranus and Neptune (e.g. [Conrath et al. 1998](#)), and has been exploited by Earth-based astronomers, space observatories (e.g., ISO, Spitzer, AKARI, Herschel), and visiting spacecraft (e.g., Voyager, Galileo, and Cassini). The short-lived dipoles induced by these collisions between free molecules (*free-to-free* interactions) generate broad and smooth spectral features around the rotational  $S(0)$  ( $354\text{ cm}^{-1}$ ) and  $S(1)$  ( $587\text{ cm}^{-1}$ ) lines. Transitions between para- $\text{H}_2$  rotational levels  $0 \rightarrow 2$  are responsible for the  $S(0)$  features (even rotational quantum numbers), and transitions between ortho- $\text{H}_2$  rotational levels  $1 \rightarrow 3$  are responsible for the  $S(1)$  feature. Measurement of the far-infrared spectrum can therefore provide constraints on the tropospheric temperatures, para- $\text{H}_2$  fractions (a tracer of atmospheric mixing, [Conrath et al. 1998](#)), and the bulk helium abundance ([Conrath & Gautier 2000](#)).

It has been common practice to only include these free-to-free contributions when calculating the opacity of giant planet atmospheres, in addition to the narrow quadrupole lines. However, sharp features near  $S(0)$  ( $354\text{ cm}^{-1}$ ) identified in Voyager IRIS  $4.3\text{-cm}^{-1}$ -resolution spectra of Jupiter and Saturn were attributed to hydrogen dimers by [Frommhold et al. \(1984\)](#) and [McKellar \(1984\)](#), and confirmed via low-temperature experiments by [McKellar \(1988\)](#). This dimeric absorption, detectable as a slight modification to the free-free absorption of the parent molecules, is the result of the formation of a weakly-bound  $(\text{H}_2)_2$  complex held together by van-der-Waals forces. The main mechanism of dimer formation and dissociation is three-body interactions, which sustain a dimer abundance determined by thermal equilibrium. To a much smaller extent, dimers may be formed during *free-to-bound* ( $\text{H}_2+\text{H}_2 \rightarrow (\text{H}_2)_2$ ) radiative transitions, which generate features redward (smaller wavenumbers) of the rotational line centre in the absorption spectrum; and dissociated during *bound-to-free* transitions ( $(\text{H}_2)_2 \rightarrow \text{H}_2+\text{H}_2$ ) that generate spectral signatures blueward (larger wavenumbers) of the line centre (e.g., from *ab initio* models by [Frommhold et al. 1984](#)). As the dimer lifetime is much longer than the short-lived free-to-free collisions, the spectral features are much narrower. Despite being one of the weakest dimers in nature, the  $(\text{H}_2)_2$  contribution was readily visible in the Voyager spectra near  $S(0)$ .

Following their identification, a series of experimental and theoretical results were presented to characterise the dimer contributions ([Schaefer 1987](#); [McKellar 1988, 1990](#); [McKellar & Schaefer 1991](#)). The strength of the dimer absorp-

tion depends on the abundance of  $\text{H}_2$ , the ortho-para ratio, and the temperature. The influence of the dimers on the spectrum is most important at low temperature, as shown in the 20-K experiments by ([McKellar & Schaefer 1991](#)). [Meyer et al. \(1989\)](#) demonstrated that the extra free-to-bound and bound-to-free transitions could alter the continuum tens of wavenumbers away from the line centre. [Carlson et al. \(1992\)](#) fitted the Meyer calculations with empirical formulae to incorporate this broadband dimer structure into the IRIS modelling, finding that this additional absorption significantly improved their fit near  $350\text{ cm}^{-1}$ . Furthermore, [Kim et al. \(1995\)](#) and [Trafton et al. \(1997\)](#) identified dimer emission in Jupiter, Saturn and Neptune near the  $\text{H}_2$  fundamental at  $2.1\text{ }\mu\text{m}$ .

However, despite these pioneering studies, subsequent analyses over the past two decades have largely omitted this additional absorption and considered only the free-to-free transitions. Analyses of giant planet infrared spectra have typically utilised the free-free  $\text{H}_2\text{-H}_2$  opacity model of [Borysow et al. \(1985\)](#), which was based on *ab initio* dipole surfaces from ([Meyer et al. 1989](#)). However, [Orton et al. \(2007\)](#) demonstrated that an error had been made in the modelling of the dipole components by [Borysow et al. \(1985\)](#), which appeared at the rotational double transitions in the absorption spectrum. [Orton et al. \(2007\)](#) carried out extensive corrected calculations, which were otherwise at the same level of theory as [Borysow et al. \(1985\)](#). Their corrected free-to-free coefficients, which were only provided (i) for normal  $\text{H}_2$  (i.e., a 3:1 mixture of ortho- $\text{H}_2$  and para- $\text{H}_2$ ) and (ii) for  $\text{H}_2$  with para and ortho states in equilibrium at the local temperature, now form the ‘Alternative’ CIA database maintained by HITRAN ([Richard et al. 2012](#)). However, [Fletcher et al. \(2017\)](#) showed that this new free-to-free calculation resulted in smaller absorption coefficients near the  $S(0)$  and  $S(1)$  lines than the original database of [Borysow et al. \(1985\)](#), which led to spurious effects when fitting Voyager/IRIS spectra of Jupiter, despite being a more accurate calculation of the free-to-free contribution. The solution requires the addition of the dimer opacity, as originally envisaged by [Frommhold et al. \(1984\)](#), [Carlson et al. \(1992\)](#) and others. This was employed by [Orton et al. \(2014a\)](#) in their analysis of Uranus’  $S(1)$  line from Spitzer data, which confirmed the existence of dimer features in Uranus’ far-infrared spectrum for the first time. In summary, use of the free-to-free absorption coefficients of [Orton et al. \(2007\)](#) in isolation will underestimate the opacity required to properly reproduce giant planet spectra. Bound-to-free and free-to-bound absorption coefficients, calculated for a range of temperatures and para- $\text{H}_2$  fractions, are also required.

Section 2 presents new calculations of the free-to-free, bound-to-free, free-to-bound and bound-to-bound  $(\text{H}_2)_2 \rightarrow (\text{H}_2)_2$  contributions to the  $\text{H}_2\text{-H}_2$  opacity for giant planet

atmospheres, extending the work of (Orton et al. 2007). Section 3 shows that the new *ab initio* model can be used to reproduce the fine-scale structure observed in high-resolution spectroscopy of the S(0) and S(1) regions on all four giant planets, using data from Cassini (Jupiter and Saturn) and Spitzer (Uranus and Neptune). We present the first observations of the S(0) dimer on Uranus; the first observation of both S(0) and S(1) dimers on Neptune; and the first observation of the S(1) dimers on Jupiter and Saturn. Inclusion of this structured dimer absorption along with the smooth CIA will be essential for interpretations of spectra from the James Webb Space Telescope.

## 2. SPECTRAL CALCULATION

The quantum mechanical calculations of the interaction-induced spectra have been divided into three categories according to the physical mechanism, each category having its own method of calculation of the  $\text{H}_2\text{-H}_2$  wave functions. The first two categories are also described briefly in Gustafsson (2017).

*Free-to-free:* This contribution is computed using the conventional method with an isotropic interaction potential (Meyer et al. 1989). The use of the isotropic potential approximation (IPA) is justified as the anisotropy has been shown to have only a small effect on the absorption coefficient for  $\text{H}_2\text{-H}_2$ , in particular around the rotational transitions that we focus on in this work (Gustafsson et al. 2003; Karman et al. 2015). A Numerov algorithm (Korn & Korn 1968) is implemented to obtain the one-dimensional continuum wave functions. The table presented by Orton et al. (2007) has been refined in the regions surrounding the S(0) and S(1) transitions,  $310\text{-}400\text{ cm}^{-1}$  and  $530\text{-}630\text{ cm}^{-1}$ , respectively, to account for the presence of fine features in the energy-dependent absorption cross section. These have to be resolved for an accurate numerical integration over energy, which is done to obtain the temperature-dependent absorption coefficient. Finally, we extend the work of Orton et al. (2007) by calculating the free-to-free absorption coefficients on a grid of ten temperatures (40-400 K) and ten para- $\text{H}_2$  fractions (0.25-1.0).

*Bound-to-free and free-to-bound:* Here the isotropic potential approximation (IPA) is also applied. The bound state wave functions are computed with a discrete variable representation (DVR) with a uniform grid (Colbert & Miller 1992) and the continuum states are computed with the Numerov algorithm. The formula for the absorption coefficient is taken from Meyer et al. (1989). A  $0.5\text{-cm}^{-1}$  empirical shift of the upper dimer level was applied for the free-to-bound transitions on the low-frequency side of the S(0) line. The shift is applied for collisions where the  $\text{H}_2$  molecules are in the  $(j_1, j_2) = (0, 0)$ ,  $(0, 1)$ , or  $(1, 0)$  rotational states. The shift was identified empirically via comparison with experimen-

tal data, but the magnitude is consistent with the comparison of these dimer levels (which are computed with the isotropic potential) with those computed using the full anisotropic potential, given below. For the upper dimer level the difference is on the order of  $0.5\text{ cm}^{-1}$ .

*Bound-to-bound:* These calculations require the inclusion of the anisotropy of the potential to give transition frequencies in agreement with those observed in the laboratory. A new program, using the DVR algorithm with an anisotropic potential, was developed to compute the absorption coefficient. The method is outlined in Appendix A.

All calculations have been carried out using the potential by Schäfer & Köhler (1989) and the dipole by Meyer et al. (1989). A more recent potential surface, which was used by Karman et al. (2015), has also been tested, but it failed to give dimer states that are consistent with the experiments.

Figs. 1, 2, and 3 compares our calculated absorption spectra surrounding the S(0) and S(1) transitions with experimental data at temperatures of 20 K (McKellar & Schaefer 1991) and 77 K (McKellar 1988). A variety of para- to ortho-hydrogen ratios have been used in these figures. The computed bound-to-bound spectrum was convolved with a triangular slit function of width  $w = 0.2\text{ cm}^{-1}$  to match the experimental resolution. The sums of the spectral contributions agree reasonably well with the experiment. For the cases of pure para-hydrogen the agreement is particularly good (Figs. 1-2). For the case of equilibrium-hydrogen (Fig. 3) the agreement is better for the S(0) transition than for the S(1) transition. This difference implies that the  $j_i > 0$  monomer rotations are more poorly described in the bound-to-free and free-to-bound cases, indicating that an anisotropic potential treatment would improve the agreement. We also note that the density was higher for the experimental measurements taken with a larger fraction of ortho-hydrogen, so that pressure broadening may have affected these spectral features.

## 3. GIANT-PLANET MODELLING

### 3.1. Sources of Data

To date, the  $(\text{H}_2)_2$  dimer absorption has only been studied near the S(0) feature in Voyager/IRIS  $4.3\text{-cm}^{-1}$  resolution spectra of Jupiter and Saturn (Frommhold et al. 1984) and were identified in  $R \sim 600$  resolution Spitzer spectra of the S(1) feature on Uranus (Orton et al. 2014a, , although no attempts were made to fit the spectral features). We utilise Cassini Composite Infrared Spectrometer (CIRS, Flasar et al. 2004) spectra of Jupiter and Saturn with a wavenumber-independent  $0.48\text{-cm}^{-1}$  spectral resolution, and Spitzer Infrared Spectrometer (IRS, Houck et al. 2004) wavelength-dependent  $R \sim 600$  spectra of Uranus and Neptune (i.e.,  $0.59\text{ cm}^{-1}$  resolution at S(0) and  $0.98\text{ cm}^{-1}$  resolution at S(1)). However, as the true spectral resolution of the high-

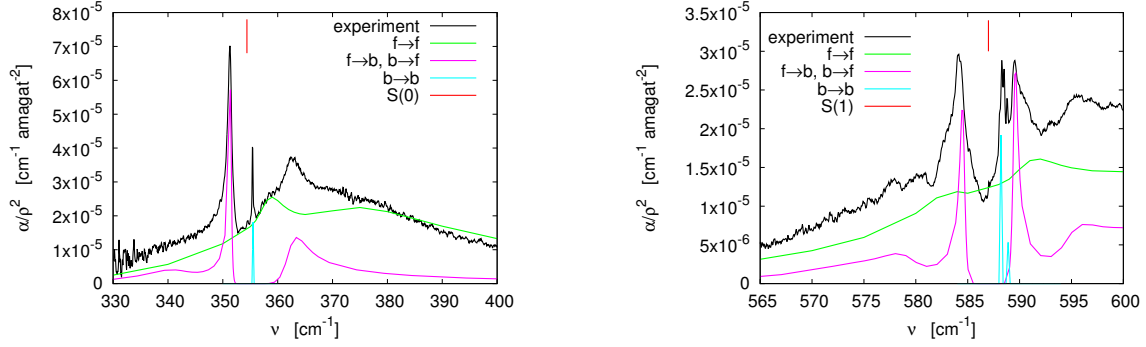


**Figure 1.** The absorption coefficient at 20 K, normalised by the square of the hydrogen density, around (a) the S(0) and (b) the S(1) transitions for pure para-hydrogen and for normal-hydrogen, respectively. The calculations are performed as described in Section 2. The line labeled ‘McKellar’ represents the laboratory measurements by McKellar & Schaefer (1991). Pressures of about 49 Torr (equivalent to a density of 0.88 amagat) and 40 Torr (equivalent to a density of 0.72 amagat) were used in experiments in (a) and (b), respectively.

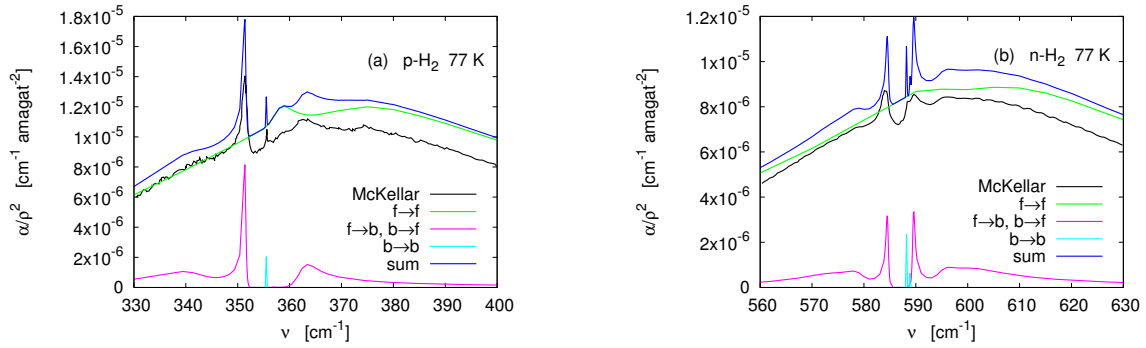


**Figure 2.** As in Fig. 1 but at a temperature of 77 K. In this case the laboratory measurements are from McKellar (1988) and were taken at number densities of 1.30 amagats and 2.45 amagats for (a) and (b), respectively.

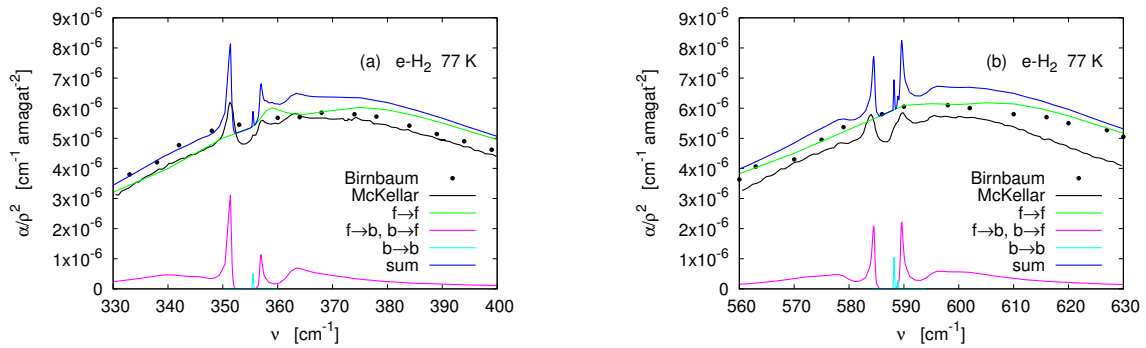


**Figure 3.** As in Fig. 2 but with equilibrium-hydrogen in both (a) and (b). The laboratory measurement by McKellar (1988) was taken at a number density of 2.63 amagats. Additional low-resolution laboratory measurements by Birnbaum (1978) are also included (circles), but these do not resolve the dimer features. However, it confirms that the overall magnitude of the calculated absorption is consistent with the experimental measurements.

resolution Spitzer modes is uncertain, we find that a resolution of  $0.48 \text{ cm}^{-1}$  is sufficient for our calculations.

*Jupiter and Saturn:* Spectra of the S(0) line were acquired by the far-IR polarising CIRS focal plane one with its circular 4.3-mrad diameter field of view, whereas spectra of the S(1) line used the 0.273-mrad square detectors of CIRS fo-

cal plane 3. Given that the detector responsivities are low in these spectral regions, large numbers of spectra were coadded to generate a single average. We ensured that the footprints of the detectors were fully on the planetary disc, and that all spectra with emission angles smaller than  $45^\circ$  were averaged. For Jupiter, we averaged spectra spanning from

November 15th 2000 - February 15th 2001 during the Cassini flyby - 850 spectra were used for S(0), 15,000 spectra for S(1). For Saturn, we averaged spectra from October 2004 to December 2016 with the same criteria, using 57,000 spectra for S(0) and 86,000 spectra for S(1). Although these large averages were necessary to improve the signal-to-noise, the resulting atmospheric profiles (temperature and para-H<sub>2</sub>) are averaged over a broad region of the planet and, in the case of Saturn, over different seasons from southern summer to northern spring. As shown in Section 4 and Fig. 4, these spectra reveal dimeric structure around S(0) on both planets and, tentatively, around S(1) on Saturn.

*Uranus and Neptune:* Spitzer/IRS acquired 7-36  $\mu\text{m}$  disc-integrated spectra of Uranus during Directors Discretionary Time on December 16-17, 2007 shortly after Uranus' equinox (program 467, full details of the data reduction process are provided by Orton et al. 2014a). Disc-integrated spectra of Neptune were acquired on November 19-20, 2005 during Spitzer's Cycle 2 (program 20500), and reduced using the same process as Orton et al. (2014a). For both planets, the observations were designed to sample multiple longitudes during a complete rotation, but we averaged all longitudes to form a single spectrum. Here we focus on high-resolution ( $R \sim 600$ ) observations in the 'Short-High' (SH) 9.95-19.30  $\mu\text{m}$  and 'Long High' (LH) 19.27-35.97  $\mu\text{m}$  ranges, revealing the S(0) and S(1) lines in Fig. 4, respectively. Note that Orton et al. (2014a) identified offsets between low- and high-resolution Uranus spectra related to flux losses from different slit sizes, and ultimately scaled the SH data to match the low-resolution modes, and abandoned the LH data from their analysis entirely. In the present work, where only narrow spectral ranges are considered to identify the dimer features, we do not find it necessary to perform such a scaling and present good fits to both SH and LH data.

*Voyager/IRIS:* To supplement the high-resolution Cassini and Spitzer observations, we also reanalyse the low-resolution ( $4.3\text{-cm}^{-1}$ ) IRIS observations of all four giant planets. These 180-2500  $\text{cm}^{-1}$  spectra were acquired by a Michelson interferometer in a series of north-south scans executed during the close flybys between 1979 and 1989. The selection criteria for the spectra and zonal averaging techniques have been previously described for Jupiter (Fletcher et al. 2017), Saturn (Fletcher et al. 2016), Uranus (Orton et al. 2015) and Neptune (Fletcher et al. 2014). Dimer features were previously identified only in the Jupiter and Saturn spectra (Frommhold et al. 1984), with the Uranus and Neptune data being too low in signal to reveal the dimer absorptions. The zonally-averaged 300-550  $\text{cm}^{-1}$  regions of these spectra are re-analysed with the new opacity database in Section 4.

### 3.2. Spectral Retrieval Model

The NEMESIS spectral retrieval algorithm (Irwin et al. 2008) was used to model the H<sub>2</sub> quadrupoles, dimers and continuum absorption on all four giant planets in Fig. 4. NEMESIS uses Newtonian iteration and an optimal estimation retrieval architecture (Rodgers 2000) to calculate planetary spectra, maximising the quality of the spectral fit whilst using constraints to prior data (in this case, vertical temperature and para-H<sub>2</sub> profiles) to ensure smooth and physically-realistic retrieved profiles. For the spatially-resolved spectra of Jupiter and Saturn, NEMESIS was used in its standard mode, computing spectra using the mean geometry (latitude and emission angle) of the spectral averages (e.g., Fletcher et al. 2009). For the disc-integrated Uranus and Neptune spectra, we employed an exponential-integral technique (Goody & Yung 1989) to compute the radiance into a hemisphere (Fletcher et al. 2014). Although the spectra explored in this paper are formed primarily by H<sub>2</sub>, He (and H<sub>2</sub>-CH<sub>4</sub> collisions, to a lesser extent), we use full atmospheric priors for each planet with tropospheric (CH<sub>4</sub>, PH<sub>3</sub>, NH<sub>3</sub>) and stratospheric species (hydrocarbons) included based on previous NEMESIS studies of Jupiter and Saturn (Fletcher et al. 2009), Uranus (Orton et al. 2014a,b) and Neptune (Fletcher et al. 2014). Although not strictly necessary in this analysis, the sources of spectral linedata for these species are located in Table 4 of Fletcher et al. (2012).

The new *ab initio* model described in Section 2 produced calculations of the interaction-induced dimer spectra (free-to-bound, bound-to-free, bound-to-bound). This was combined with updated estimates of the free-to-free H<sub>2</sub>-H<sub>2</sub> contribution, the H<sub>2</sub>-He contribution from Borysow et al. (1988), and H<sub>2</sub>-CH<sub>4</sub> and CH<sub>4</sub>-CH<sub>4</sub> contributions from Borysow & Frommhold (1986, 1987). Extending the work of Orton et al. (2007), the new free-to-free H<sub>2</sub> and He contributions, as well as the dimer contributions, were calculated for a range of para-H<sub>2</sub> fractions between 0.25 and 1.0, and for temperatures from 40 to 400 K. These tables are then interpolated during the temperature and para-H<sub>2</sub> retrievals to calculate the atmospheric transmission. In addition, we include the H<sub>2</sub> quadrupole transitions from the *ab initio* calculations described in Rothman et al. (2013), which are in agreement with recent experimental results of Campargue et al. (2012). Specifically, S(0) occurs at 354.3732  $\text{cm}^{-1}$  with an intensity of  $1.664 \times 10^{-28} \text{ cm}^{-1}/\text{molec cm}^{-2}$ ; S(1) occurs at 587.0320  $\text{cm}^{-1}$  with an intensity of  $2.657 \times 10^{-27} \text{ cm}^{-1}/\text{molec cm}^{-2}$ . Both have a width of 0.0017  $\text{cm}^{-1}/\text{atm}$  (Reuter & Sirota 1994) and temperature dependence  $T^n$  where  $n = 0.75$ . Full vertical profiles of  $T(p)$  and para-H<sub>2</sub> ( $f_p(p)$ ) were retrieved independently to reproduce the eight spectral regions shown in Fig. 4. Note that retrievals over a broader spectral range would be required to fully constrain these atmospheric profiles, whereas the present study aims to show that the fine-scale dimeric structure can be adequately reproduced.



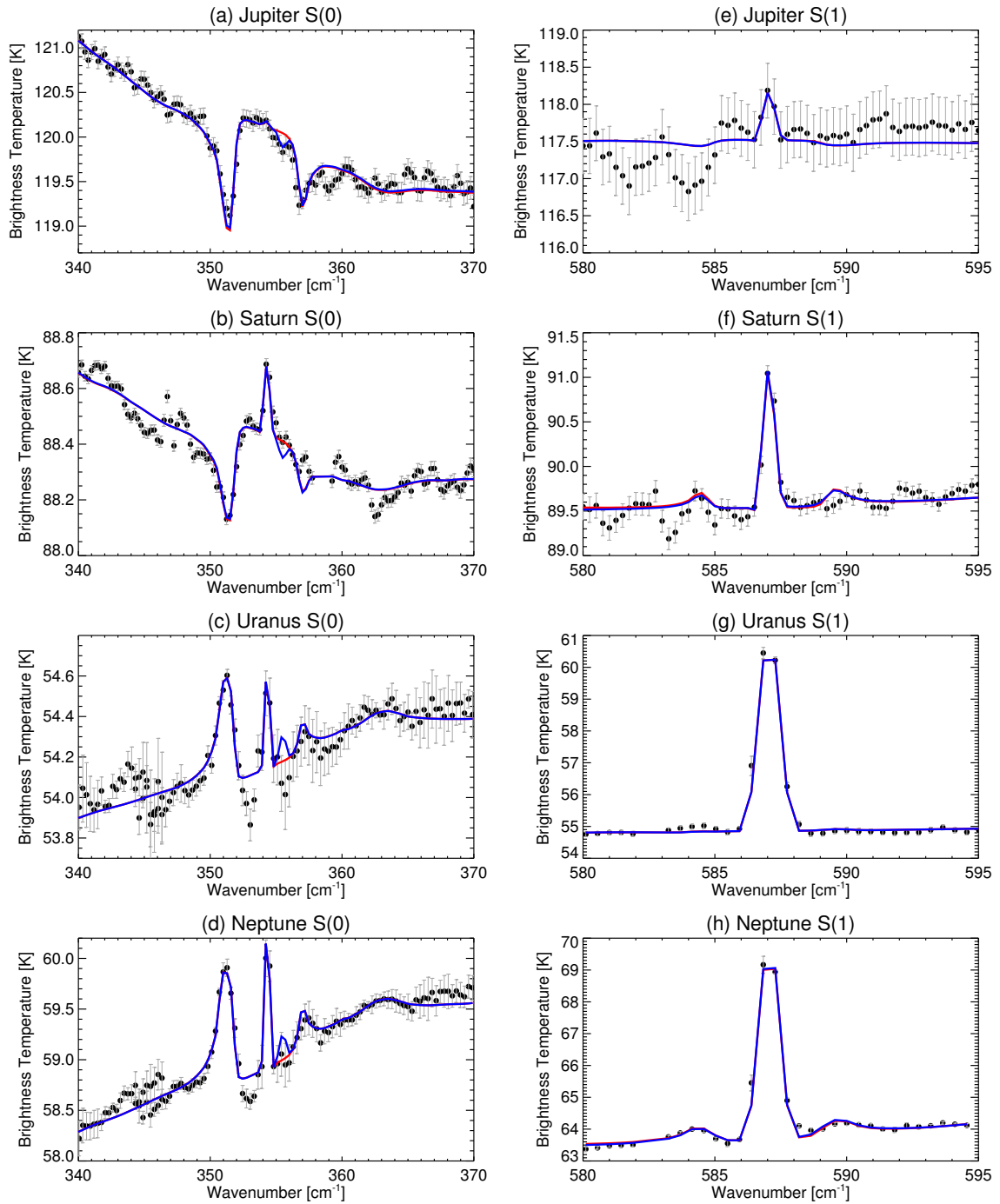


**Figure 4.** Spectral fits to the S(0) and S(1) lines detected on all four giant planets, using Cassini data for Jupiter and Saturn and Spitzer data for Uranus and Neptune.

## 4. RESULTS AND DISCUSSION

### 4.1. High-resolution dimer structure

Fig. 4 compares model spectra to the high-resolution Cassini and Spitzer measurements in the regions within a few tens of wavenumbers of the quadrupole transitions. On Jupiter and Saturn, the CIRS data provided better signal-to-noise near the S(0) line than the S(1) line, permitting identi-

fication of the main free-to-bound ( $351.1 \text{ cm}^{-1}$ ,  $l = 2 \rightarrow 1$ ) and bound-to-free ( $357 \text{ cm}^{-1}$ ,  $l = 1 \rightarrow 2$ ) transitions  $\sim 3 \text{ cm}^{-1}$  either side of the quadrupole. These features are seen in absorption, as the strongest dimer absorptions are sensing higher, cooler altitudes near to the tropopause on both planets. The asymmetry in the line intensities between these two features (shown in Fig. 1-3 for the S(0) line) is related to the boson symmetry of para- $\text{H}_2$  (Frommhold et al. 1984).

Additional undulations in the continuum can be seen near  $346\text{ cm}^{-1}$  and  $363\text{ cm}^{-1}$  (free-to-bound  $l = 3 \rightarrow 0$  and bound-to-free  $l = 0 \rightarrow 3$ , respectively) that contribute to the overall absorption provided by the broad free-free transition. Although these gas-giant  $S(0)$  dimers have been previously studied at low resolution from Voyager/IRIS (see Section 4.2, Frommhold et al. 1984; McKellar 1984), this is the first observation at a sufficient spectral resolution to resolve their line shapes.

The CIRS observations near  $587\text{ cm}^{-1}$  have much poorer noise characteristics near the edge of the detector responsivity curve, so little is identifiable beyond the central quadrupole lines. Fig. 4e-f shows that the expected dimer structure is within the uncertainty on the measurement, but we expect jovian absorption and saturnian emission near  $584.5\text{ cm}^{-1}$  and  $589.5\text{ cm}^{-1}$ ,  $\sim 2.5\text{ cm}^{-1}$  either side of the quadrupole emission. Saturn's  $S(1)$  dimer appears in emission rather than absorption because it senses altitudes just above the tropopause, in the region where temperature begins to increase with altitude in the lower stratosphere.

The general appearance of the dimer absorption near  $S(0)$  changes character considerably for Uranus and Neptune, where both the data and model indicate that the main free-to-bound and bound-to-free transitions  $\sim 3\text{ cm}^{-1}$  from the line centre are sensing stratospheric altitudes, warmer than the surrounding free-free transitions. The  $351\text{-cm}^{-1}$  feature almost matches the intensity of the quadrupole line itself. The measured spectrum becomes increasingly noisy shortward of  $347\text{ cm}^{-1}$  due to an overlap of modes in the Spitzer LH setting. However, this cannot account for the extremely poor fit to the spectrum between  $352\text{-}354\text{ cm}^{-1}$ , where no dimer transitions exist to add to the absorption of the free-free contribution. The data suggest that excess absorption could be required to make the spectrum sense higher, cooler altitudes towards the tropopause, but experiments with *ad hoc* modifications to the dimer database failed to offer improvements. Given that there is no evidence of excess absorption in the gas giant spectra, and that there are additional deviations in the Spitzer ice giant measurements that aren't accounted for by our model, it is likely that this mismatch is unrelated to the dimer spectra and is simply the result of noisy data. New measurements of the dimer features with JWST (see Section 5) or other far-IR facilities such as SOFIA should help to resolve this conundrum.

Ice giant dimer features near  $S(1)$  are significantly weaker, owing to the quasi-isothermal tropopause regions to which the dimers are sensitive. Uranus'  $S(1)$  dimers were first identified by Orton et al. (2014a), but no attempt was made to fit the discrete structures. In Fig. 4g, the free-to-bound transition near  $584.5\text{ cm}^{-1}$  is present in the data, but our model struggles to fit it due to the weakness of the bound-to-free transition near  $589.5\text{ cm}^{-1}$  (the spectral fit is a compromise

over fitting the whole region). The signal-to-noise ratio of the Spitzer data is excellent here, so this could represent a deficiency of the model. However, the model is more successful at fitting Neptune's  $S(1)$  line and dimer structure, which is stronger than for Uranus and shows equal strength in the free-to-bound and bound-to-free transitions. We conclude that the new *ab initio* model provides adequate spectral fits to  $S(0)$  and  $S(1)$  features on all four giant planets, despite some model-data discrepancies that we hope to constrain with improved future measurements.

Finally, we note that two spectral models are shown in Fig. 4 - one without bound-to-bound transitions (red) and one with them (blue). Although the bound-to-bound transitions were clearly present in the experimental data (Fig. 1-3), their influence near  $S(1)$  is negligible, and their importance on the giant planet  $S(0)$  spectra is unclear. On Jupiter, the addition of the bound-bound opacity does improve the fit near  $355.5\text{ cm}^{-1}$ . However, on Saturn, Uranus, and Neptune, the inclusion of the bound-bound data actually worsens the fits. We have chosen to show both options, although the requirement for the bound-bound contribution remains unclear.

#### 4.2. Low-resolution: Voyager/IRIS

Spectral modelling of Voyager/IRIS  $300\text{-}550\text{ cm}^{-1}$  spectra of Jupiter by Fletcher et al. (2017) had revealed a problem when the free-to-free transitions of Orton et al. (2007) were used in isolation, as they under-predicted the amount of collision-induced opacity required to fit the data with a physically-plausible atmospheric structure. This present study was prompted by the need to add dimer opacity to the free-free continuum to explain the Voyager data. Ironically, the error in the calculation of some of the free-free components by Borysow et al. (1985) had led to an opacity dataset that was closer to reality. We repeat the Voyager/IRIS fitting using three assumptions for the  $\text{H}_2\text{-H}_2$  opacity: (i) the original free-free database of Borysow et al. (1985), (ii) the newer free-free database of Orton et al. (2007), and (iii) the complete free-to-free, free-to-bound, bound-to-free and bound-to-bound database of this work.

The quality of the IRIS spectral fits using the latter database is shown for all four planets in Fig. 5. For the purpose of this plot, we averaged all Voyager-1 IRIS Jupiter and Saturn spectra within  $\pm 30^\circ$  latitude of the equator, whereas for Uranus and Neptune we averaged all available Voyager-2 IRIS spectra from pole to pole, filtering for any corrupted measurements. Dimer features near  $S(0)$  are clearly identifiable and well reproduced for Jupiter and Saturn (Frommhold et al. 1984), but are indistinguishable above the IRIS noise for Uranus and Neptune.

Fig. 6 shows the consequences of using the three different CIA databases on retrievals of temperature and para- $\text{H}_2$  ( $f_p$ ) from Voyager IRIS Jupiter spectra. As shown in Fletcher

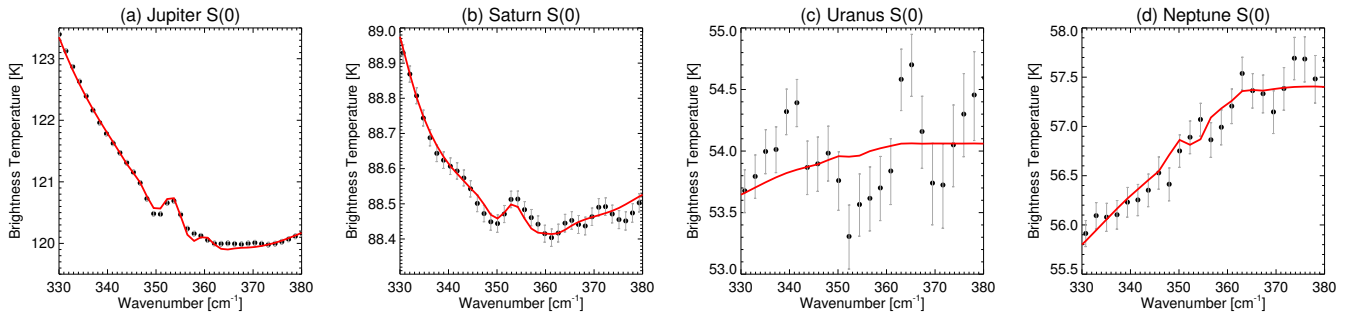


**Figure 5.** Large averages of Voyager IRIS spectra (black circles with standard errors on the mean) compared to the spectral model with all dimer transitions included (red line). Dimer absorption is clearly visible for Jupiter and Saturn observations, whereas the features are indistinguishable above the noise for Uranus and Neptune.

et al. (2017), the use of the free-free continuum of Orton et al. (2007) (Fig. 6c), without the additional absorption from the dimers near the S(0) and S(1) peaks, results in temperature retrievals with sharp lapse rates and low temperatures ( $T < 106$  K) near the tropopause. In addition, the para- $H_2$  fraction is larger ( $f_p = 0.33 - 0.34$ ) as the spectral model attempted to increase the radiance at  $350\text{ cm}^{-1}$  by increasing the  $f_p$ , resulting in a strongly sub-equilibrium atmosphere (i.e., para- $H_2$  exceeds that expected from equilibrium). The goodness-of-fit was also significantly worse in the free-free case, by a factor of three. Note that we detected a  $0.9\text{-cm}^{-1}$  offset between our spectral model and the Voyager-1 IRIS Jupiter data (which was also present in the analysis of Fletcher et al. 2017) which was not present in the Cassini and Spitzer comparisons. The IRIS data in Fig. 5 have been shifted in wavenumber to compensate. With the new dimer database, the retrieved tropospheric temperatures are smoother, with a minimum  $T \sim 110$  K and slightly lower  $f_p = 0.32 - 0.33$  leading to para- $H_2$  conditions closer to equilibrium (albeit perturbed by equatorial upwelling and polar subsidence, as described by Conrath et al. 1998; Fletcher et al. 2017). This comes close to matching the calculations using the original database of Borysow et al. (1985), where some of the free-free components had been overestimated.

The same exercise was repeated for the IRIS Saturn data (Fletcher et al. 2016). Although the temperatures retrieved using the three compilations were similar (within  $\sim 1$  K), the para- $H_2$  fraction altered by  $\sim 0.03$  in the upper troposphere. As was the case for Jupiter, this caused the calculation with only the free-free database of Orton et al. (2007) to appear strongly sub-equilibrium (i.e., more para- $H_2$  required to increase the absorption near S(0)), whereas the dimeric absorption fulfils this role in our new calculation, bringing the atmosphere closer to equilibrium, albeit with seasonal north-south gradients in Saturn’s para- $H_2$  described by Fletcher et al. (2016). For Uranus and Neptune, where only the  $200\text{-}400\text{ cm}^{-1}$  offer any constraint (and there is no sensitivity to the S(1) at all), the differences in the retrieved temperatures and para- $H_2$  were negligible and the dimer structure near

$354\text{ cm}^{-1}$  was not visible in the Voyager/IRIS  $4.3\text{-cm}^{-1}$ -resolution data (Fig. 5c-d).

## 5. CONCLUSIONS

The purely free-to-free  $H_2\text{-}H_2$  collision-induced absorption tables of Orton et al. (2007), which are included in the ‘Alternate’ directory of HITRAN 2012 (Richard et al. 2012), should not be used in isolation when fitting mid- and far-infrared spectra in the vicinity of the S(0) and S(1) lines. Instead, we propose that they should be combined with the present refined opacity offered by free-to-free, free-to-bound, bound-to-free and bound-to-bound  $H_2\text{-}H_2$  transitions within  $\pm 50\text{ cm}^{-1}$  of the line centres. A new *ab initio* model, using the isotropic interaction potential approximation and a denser energy grid than previous studies, is used to calculate the opacity provided by the former three types of transitions for a range of temperatures and para- $H_2$  fractions. Similarly, the opacity contribution from bound-to-bound transitions is computed with the full anisotropic interaction potential. This model is validated via comparison to laboratory measurements at 20 and 77 K (McKellar & Schaefer 1991; McKellar 1988), and then used in radiative transfer calculations to simulate the spectra of the four giant planets.

We find that we can reproduce the low-resolution ( $4.3\text{ cm}^{-1}$ ) dimer signatures that had been previously identified in Jupiter and Saturn Voyager spectra by McKellar (1984), and that the additional continuum absorption resolves the problems that were identified by Fletcher et al. (2017) when using the free-free calculations of Orton et al. (2007) in isolation. Observations at higher spectral resolutions ( $0.5\text{-}1.0\text{ cm}^{-1}$ ) were compiled from Cassini Composite Infrared Spectrometer (CIRS) observations of Jupiter and Saturn and Spitzer Infrared Spectrometer (IRS) observations of Uranus and Neptune. The model-data comparison reveals the presence of dimer absorption near S(0) on all four planets at high spectral resolution, and near S(1) on Uranus and Neptune (the structure is lost in the data uncertainty on Jupiter and Saturn). Dimeric transitions appear in absorption on the gas gi-



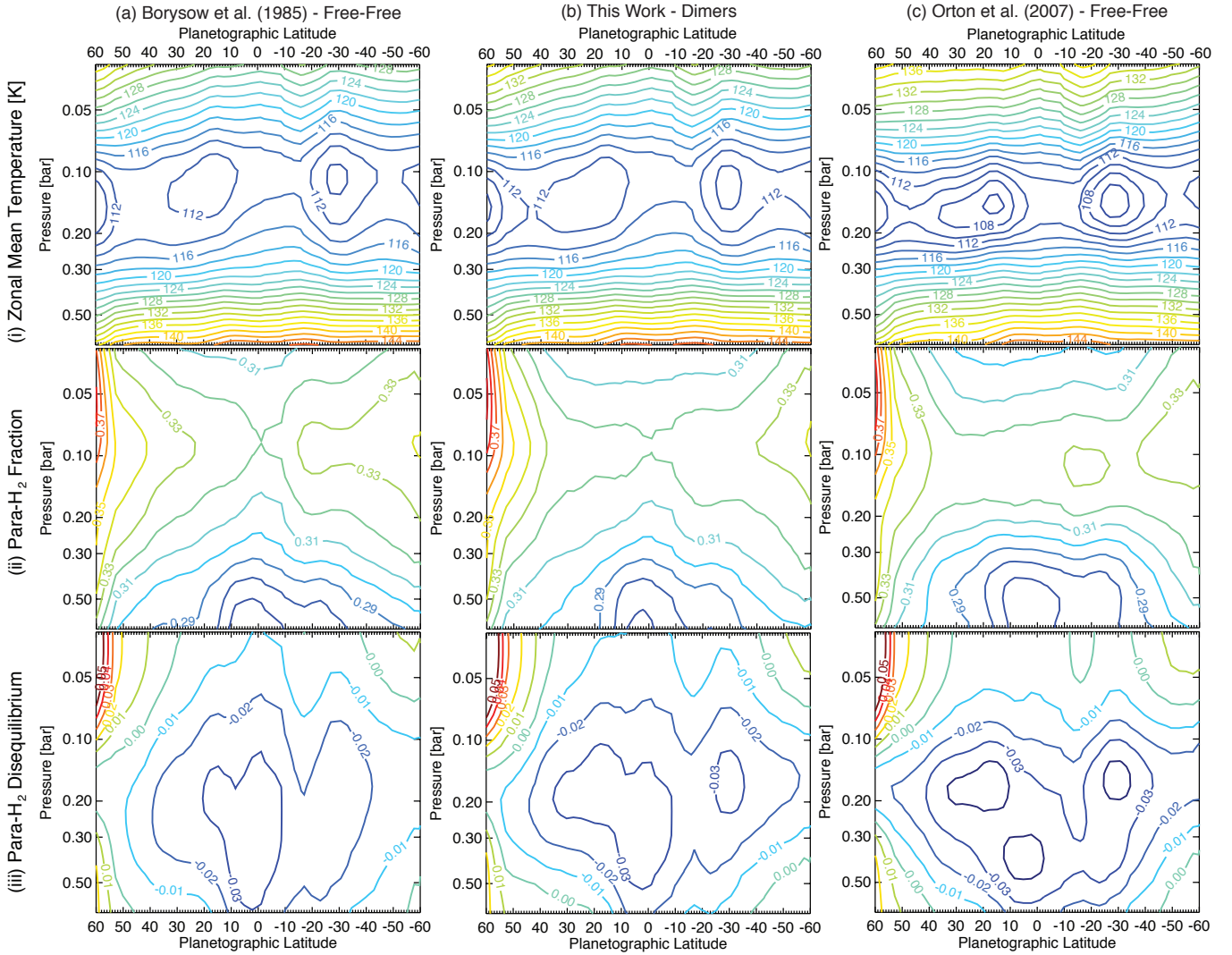


**Figure 6.** Comparison of retrieved (i) tropospheric temperatures; (ii) para-H<sub>2</sub> fraction; and (iii) difference between para-H<sub>2</sub> and equilibrium. More negative values in the bottom row indicate more para-H<sub>2</sub> than expected from equilibrium (i.e., sub-equilibrium conditions), potentially associated with upwelling motions. The results are compared between calculations using (a) the free-free continuum absorption of Borysov et al. (1985), (b) the new compilation with dimer absorption; and (c) the free-free continuum absorption of Orton et al. (2007).

ants, where they sense the upper troposphere, and in emission on the ice giants, where they sense the lower stratosphere.

Fits to the data are adequate but not perfect. For example, the importance of bound-to-bound transitions is unclear, as they improve the fit for Jupiter but not for the other giant planets. Secondly, both Uranus and Neptune have model-data discrepancies between the quadrupole at  $354.5\text{ cm}^{-1}$  and the primary dimer feature at  $351\text{ cm}^{-1}$  that we cannot account for using the *ab initio* model. It should be noted that the spectral calculations described in this work account only for binary interactions (between two hydrogen molecules), and not ternary or higher-order interactions. The sharp dimer features correspond to quantum states that are rather long-lived, and thus may be sensitive to these additional interactions, which is a possible source of error in the present

modelling work. Currently, ternary and higher-order interactions cannot be treated well with quantum mechanics, which would be necessary in the case of hydrogen. One has to resort to classical mechanical treatments (see, e.g., Hartmann et al. 2011; Fakhardji & Gustafsson 2017), which are typically well-suited for higher mass molecules such as CO<sub>2</sub> or N<sub>2</sub>. Nevertheless, the binary theory and isotropic potential approximation are able to reproduce much of the fine-scale structure observed in the giant planet spectra presented in this work.

It is possible that better observational data, with a higher sensitivity and spectral sampling, will help resolve these discrepancies. The James Webb Space Telescope, when it launches in 2019, will provide exquisite spectral capabilities in the  $5\text{-}30\ \mu\text{m}$  range using the MIRI integral field units

(Wells et al. 2015). Unfortunately, the collision-induced continuum from Jupiter and Saturn are likely to cause detector saturation (although wavelengths shortward of 11 and 16  $\mu\text{m}$  are likely to be accessible on Jupiter and Saturn, respectively). However, no saturation is expected for Uranus and Neptune, where both S(0) and S(1) will be available for further study at spectral resolutions of  $R \sim 3000$  (channel 3LONG, 15.4-18.1  $\mu\text{m}$ ) and  $R \sim 1600$  (channel 4LONG, 24.0-28.5  $\mu\text{m}$ ). Observations of all four giant planets are scheduled as part of the Guaranteed Time Program of H. Hammel and will provide an excellent test of the new dimer spectra provided in this study. Finally, given the importance of this spectral range in determining the helium abundances on the giant planets via remote sensing (e.g., Conrath & Gautier 2000), we hope that this new dimer spectral database will be of use to the wider community.

Fletcher was supported by a Royal Society Research Fellowship and European Research Council Consolidator Grant (under the European Union's Horizon 2020 research and innovation programme, grant agreement No 723890) at the University of Leicester. Gustafsson acknowledges support from the Knut and Alice Wallenberg Foundation. Orton was supported by funding from the National Aeronautics and Space Administration to the Jet Propulsion Laboratory, California Institute of Technology. The new free-to-free, free-to-bound, bound-to-free and bound-to-bound opacity tables are all available at the following address: <https://doi.org/10.5281/zenodo.1095503>.

*Facilities:* Cassini, Spitzer, Voyager

## APPENDIX

### A. BOUND-TO-BOUND SPECTRA

The bound states are computed with a discrete variable representation (DVR) on a uniform grid (Colbert & Miller 1992). The formulas outlined below are for the case of two distinguishable hydrogen molecules, i.e., a complex consisting of one para- $\text{H}_2$  and one ortho- $\text{H}_2$ . At the end we will describe the modifications needed to treat a complex consisting of two identical hydrogen molecules. We will also consider the hydrogen molecules as rigid rotors, as they are throughout this work. Under those conditions the Hamiltonian for two hydrogen molecules, with centres of mass separated by the vector  $\mathbf{R}$ , is:

$$H(\hat{\mathbf{r}}_1, \hat{\mathbf{r}}_2, \mathbf{R}) = H^{\text{mol}}(\hat{\mathbf{r}}_1) + H^{\text{mol}}(\hat{\mathbf{r}}_2) - \frac{\hbar^2}{2m} \nabla_{\mathbf{R}}^2 + V(\hat{\mathbf{r}}_1, \hat{\mathbf{r}}_2, \mathbf{R}) \quad (\text{A1})$$

where the orientations of the two diatoms are given by the unit vectors  $\hat{\mathbf{r}}_1$  and  $\hat{\mathbf{r}}_2$ .  $V$  is the interaction potential and  $m$  is the bimolecular reduced mass. The wave function is expanded in angular basis functions according to:

$$\Psi_{JM}(\hat{\mathbf{r}}_1, \hat{\mathbf{r}}_2, \mathbf{R}) = \sum_{\beta} \frac{1}{R} F_{\beta}^J(R) Y_{j_1 j_2 j l}^{JM}(\hat{\mathbf{r}}_1, \hat{\mathbf{r}}_2, \hat{\mathbf{R}}) \quad (\text{A2})$$

where  $\beta$  is shorthand for the quantum numbers  $(j_1 j_2 j l)$  and  $Y_{j_1 j_2 j l}^{JM}$  is the vector coupling function:

$$Y_{j_1 j_2 j l}^{JM}(\hat{\mathbf{r}}_1, \hat{\mathbf{r}}_2, \hat{\mathbf{R}}) = \sum_{m_1 m_2 m_j m_l} C(j_1, j_2, j; m_1, m_2, m_j) C(j, l, J; m_j, m_l, M) \\ \times Y_{j_1 m_1}(\hat{\mathbf{r}}_1) Y_{j_2 m_2}(\hat{\mathbf{r}}_2) Y_{l m_l}(\hat{\mathbf{R}}), \quad (\text{A3})$$

corresponding to  $\mathbf{J} = \mathbf{j} + \mathbf{l}$  and  $\mathbf{j} = \mathbf{j}_1 + \mathbf{j}_2$ . The angular momentum quantum numbers  $\mathbf{j}_1$  and  $\mathbf{j}_2$  correspond to the diatomic rotations, and  $\mathbf{l}$  and  $\mathbf{J}$  are the end-over-end and total angular momenta, respectively. The factors  $C$  are Clebsch-Gordan coefficients. The potential is also expanded in spherical harmonics as in Gustafsson et al. (2003) and then the expansion (A2) and the Hamiltonian (A1) yields the DVR-matrix Hamiltonian:

$$H_{\alpha\alpha'\beta\beta'}^J = \left( E_{j_1}^{\text{mol}} + E_{j_2}^{\text{mol}} + \frac{\hbar^2 l(l+1)}{2mR_{\alpha}^2} \right) \delta_{\alpha\alpha'} \delta_{\beta\beta'} + T_{\alpha\alpha'} \delta_{\beta\beta'} + V_{\beta\beta'}^J(R_{\alpha}) \delta_{\alpha\alpha'} \quad (\text{A4})$$

with the kinetic energy matrix:

$$T_{\alpha\alpha'} = \frac{\hbar^2}{2m \Delta R^2} (-1)^{\alpha-\alpha'} \begin{cases} \frac{\pi^2}{3} - \frac{1}{2\alpha^2} & \alpha = \alpha' \\ \frac{2}{(\alpha-\alpha')^2} - \frac{2}{(\alpha+\alpha')^2} & \alpha \neq \alpha' \end{cases} \quad (\text{A5})$$

where the uniform DVR grid has a spacing  $\Delta R = (R_{\text{max}} - R_{\text{min}})/N$  and corresponding grid points:  $R_{\alpha} = R_{\text{min}} + \alpha \cdot \Delta R$  where  $\alpha = 1, 2, \dots, (N-1)$ . The Hamiltonian in Eq. (A4) is independent of the quantum number  $M$  (Green 1975) and thus the

**Table 1.** Statistical weights  $g_{j_1 j_2}^\epsilon(f_p)$  for different combinations of para- and ortho-H<sub>2</sub> and different symmetries  $\epsilon$ 

$j_1$	$j_2$	$\epsilon$	$g_{j_1 j_2}^\epsilon(f_p)$
even	even	+	$f_p^2$
even	even	-	0
odd	odd	+	$\frac{2}{3}(1-f_p)^2$
odd	odd	-	$\frac{1}{3}(1-f_p)^2$
even/odd	odd/even		$f_p(1-f_p)$

eigenvectors and eigenenergies are also  $M$ -independent. The H<sub>2</sub> rotational energies  $E_{j_i}^{\text{mol}}$  are taken from [Stoicheff \(1957\)](#) and they are shifted so that  $E_0^{\text{mol}} = 0$ . The potential matrix element is:

$$V_{\beta\beta'}^J(R_\alpha) = \sum_{\gamma_1\gamma_2\gamma} V_{\gamma_1\gamma_2\gamma}(R_\alpha) e_{\gamma_1\gamma_2\gamma}(j_1, j_2, j, l, j'_1, j'_2, j', l'; J), \quad (\text{A6})$$

where the coefficient,  $e_{\gamma_1\gamma_2\gamma}$ , and the expansion of  $V$  is given in [Gustafsson et al. \(2003\)](#). The Schrödinger equation is solved through diagonalisation of the Hamiltonian (A4) and  $(N-1)N_\beta$  eigenvectors,  $F_{\beta k}^J(R_\alpha)$ , and eigenenergies,  $E_k^J$  are obtained.  $N_\beta$  is the number of angular momentum basis functions in the expansion, Eq. (A2). The diagonalisation is done with the DSYEV routine from LAPACK ([Anderson et al. 1999](#)).

With the eigenstates determined as described above the absorption coefficient can be computed from the matrix elements of the interaction-induced electric dipole moment. The temperature dependent absorption coefficient is (see e.g. [Karman et al. \(2015\)](#)):

$$\begin{aligned} \frac{\alpha(\nu, T)}{\rho^2} &= \sum_{E_{k'}^{J'} > E_k^J} \frac{4\pi^3}{hc} \nu_{k'k}^{J'J} \left( 1 - \exp\left(-\frac{E_{k'}^{J'} - E_k^J}{k_B T}\right) \right) \frac{h^3}{(2\pi m k_B T)^{3/2}} g_{j_1 j_2}^\epsilon(f_p) \\ &\times \exp\left(-\frac{E_k^J - E_{\text{asympt}}}{k_B T}\right) \left| M_{kk'}^{JJ'} \right|^2 \left( \frac{1}{w} - \frac{\max(\nu - \nu_{k'k}^{J'J}, \nu_{k'k}^{J'J} - \nu)}{w^2} \right) \end{aligned} \quad (\text{A7})$$

where  $\nu$  is the wavenumber of the radiation in  $\text{cm}^{-1}$  and  $\nu_{k'k}^{J'J} = \frac{E_{k'}^{J'} - E_k^J}{hc}$  is the transition wavenumber.  $E_{\text{asympt}}$  is the low-est asymptotic energy when the two hydrogen molecules are separated, i.e. for the case of one ortho- and one para-hydrogen  $\frac{E_{\text{asympt}}}{hc} = \frac{E_1^{\text{mol}}}{hc} \approx 118.5 \text{ cm}^{-1}$ . The last parenthesis in Eq. (A7) produces a triangular line profile of width  $w$ . The fraction of para-H<sub>2</sub> in the gas is  $f_p$ , which is 1, 0.5, 0.25 for pure para-H<sub>2</sub>, equilibrium-H<sub>2</sub> at 77 K, and normal-H<sub>2</sub>, respectively. Those are the cases considered in the comparison with laboratory measurements in section 2. The statistical weight  $g$  is given in table 1. The matrix elements of the dipole moment is:

$$M_{kk'}^{JJ'} = \sum_{\beta} \sum_{\beta'} \sum_{\alpha} \sum_{\lambda_1 \lambda_2 \lambda L} F_{\beta k}^J(R_\alpha) A_{\lambda_1 \lambda_2 \lambda L}(R_\alpha) F_{\beta' k'}^{J'}(R_\alpha) d_{\lambda_1 \lambda_2 \lambda L}^{\beta J \beta' J'} \quad (\text{A8})$$

where the coefficient  $d_{\lambda_1 \lambda_2 \lambda L}^{\beta J \beta' J'}$  is given in [Gustafsson et al. \(2003\)](#). Note that the coefficient  $d_{\lambda_1 \lambda_2 \lambda L}^{\beta J \beta' J'}$  includes a factor  $1/\sqrt{3}$ , which would otherwise have appeared as 1/3 in Eq. (A7). The spherical dipole components  $A_{\lambda_1 \lambda_2 \lambda L}$  come from the expansion of the electric dipole moment:

$$\mu_z(\hat{\mathbf{r}}_1, \hat{\mathbf{r}}_2, \mathbf{R}) = \frac{(4\pi)^{3/2}}{\sqrt{3}} \sum_{\lambda_1 \lambda_2 \lambda L} A_{\lambda_1 \lambda_2 \lambda L}(R) Y_{\lambda_1 \lambda_2 \lambda L}^{10}(\hat{\mathbf{r}}_1, \hat{\mathbf{r}}_2, \hat{\mathbf{R}}) \quad (\text{A9})$$

where only the  $z$ -component has to be considered because the  $z$ -direction defines the angular momentum quantization axis in a space fixed frame of reference ([Julienne 1982](#)).

For the case of dimers consisting of two identical molecules (para-para or ortho-ortho) the wave functions have to be symmetrized. The symmetry parameter  $\epsilon$  is + and - for symmetric and antisymmetric wave functions, respectively. Two of the formulas above have to be modified accordingly. In Eq. (A6) the coefficient  $e_{\gamma_1\gamma_2\gamma}$  has to be replaced by its  $\epsilon$ -dependent version, and the same goes for  $d_{\lambda_1 \lambda_2 \lambda L}$  in Eq. (A8). The  $\epsilon$ -dependent coefficients are given in the appendix of [Gustafsson et al. \(2003\)](#). Finally, the dipole selection rules have to be obeyed for all transitions included in the calculation of the absorption coefficient according to Eqs. (A7) and (A8). These are the following:

- Total angular momentum:  $J' = J; J \pm 1$ .
- $j_i$  and  $j'_i$  are both even or both odd for  $i=1$  or  $2$ .
- Parity must change, implying that  $l$  changes from odd to even or vice versa.
- In the case of identical molecules the symmetry,  $\epsilon$ , is conserved.

## REFERENCES

- Anderson, E., Bai, Z., Bischof, C., et al. 1999, LAPACK Users' Guide, 3rd edn. (Philadelphia, PA: Society for Industrial and Applied Mathematics)
- Birnbaum, G. 1978, *J. Quant. Spectro. Rad. Trans.*, 19, 51
- Borysow, A., & Frommhold, L. 1986, *Astrophys. J.*, 304, 849
- . 1987, *Astrophys. J.*, 318, 940
- Borysow, J., Frommhold, L., & Birnbaum, G. 1988, *Astrophys. J.*, 326, 509
- Borysow, J., Trafton, L., Frommhold, L., & Birnbaum, G. 1985, *Astrophys. J.*, 296, 644
- Campargue, A., Kassi, S., Pachucki, K., & Komasa, J. 2012, *Physical Chemistry Chemical Physics (Incorporating Faraday Transactions)*, 14, 802
- Carlson, B. E., Laxis, A. A., & Rossow, W. B. 1992, *Astrophys. J.*, 393, 357
- Colbert, D. T., & Miller, W. H. 1992, *JChPh*, 96, 1982
- Conrath, B. J., & Gautier, D. 2000, *Icarus*, 144, 124
- Conrath, B. J., Gierasch, P. J., & Ustinov, E. A. 1998, *Icarus*, 135, 501
- Fakhardji, W., & Gustafsson, M. 2017, in *Journal of Physics Conference Series*, Vol. 810, *Journal of Physics Conference Series*, 012031
- Flasar, F. M., Kunde, V. G., Abbas, M. M., et al. 2004, *Space Science Reviews*, 115, 169
- Fletcher, L. N., de Pater, I., Orton, G. S., et al. 2014, *Icarus*, 231, 146
- Fletcher, L. N., de Pater, I., Reach, W. T., et al. 2017, *Icarus*, 286, 223
- Fletcher, L. N., Irwin, P. G. J., Achterberg, R. K., Orton, G. S., & Flasar, F. M. 2016, *Icarus*, 264, 137
- Fletcher, L. N., Orton, G. S., Teanby, N. A., & Irwin, P. G. J. 2009, *Icarus*, 202, 543
- Fletcher, L. N., Hesman, B. E., Achterberg, R. K., et al. 2012, *Icarus*, 221, 560
- Frommhold, L., Samuelson, R., & Birnbaum, G. 1984, *ApJ Letters*, 283, L79
- Goody, R. M., & Yung, Y. L. 1989, *Atmospheric radiation : theoretical basis (Atmospheric radiation : theoretical basis, 2nd ed., by Richard M. Goody and Y.L. Yung. New York, NY: Oxford University Press, 1989)*
- Green, S. 1975, *JChPh*, 62, 2271
- Gustafsson, M. 2017, *J. Phys. Conf. Ser.*, 810, 012017
- Gustafsson, M., Frommhold, L., Bailly, D., Bouanich, J.-P., & Brodbeck, C. 2003, *JChPh*, 119, 12264
- Hartmann, J.-M., Boulet, C., & Jacquemart, D. 2011, *Journal of Chemical Physics*, 134, 094316
- Houck, J. R., Roellig, T. L., van Cleve, J., et al. 2004, *ApJS*, 154, 18
- Irwin, P., Teanby, N., de Kok, R., et al. 2008, *Journal of Quantitative Spectroscopy and Radiative Transfer*, 109, 1136
- Julienne, P. S. 1982, *PhRvA*, 26, 3299
- Karman, T., van der Avoird, A., & Groenenboom, G. C. 2015, *Journal of Chemical Physics*, 142, 084305
- Kim, S. J., Trafton, L. M., Geballe, T. R., & Slanina, Z. 1995, *Icarus*, 113, 217
- Korn, G. A., & Korn, T. M. 1968, *Mathematical handbook for scientists and engineers, 2nd edn. (New York: McGraw-Hill book company)*
- McKellar, A. R. W. 1984, *Canadian Journal of Physics*, 62, 760
- . 1988, *Astrophys. J. Lett.*, 326, L75
- . 1990, *Journal of Chemical Physics*, 92, 3261
- McKellar, A. R. W., & Schaefer, J. 1991, *Journal of Chemical Physics*, 95, 3081
- Meyer, W., Borysow, A., & Frommhold, L. 1989, *PhRvA*, 40, 6931
- Meyer, W., Frommhold, L., & Birnbaum, G. 1989, *Physical Review A*, 39, 2434
- Orton, G. S., Fletcher, L. N., Encrenaz, T., et al. 2015, *Icarus*, 260, 94
- Orton, G. S., Gustafsson, M., Burgdorf, M., & Meadows, V. 2007, *Icarus*, 189, 544
- Orton, G. S., Fletcher, L. N., Moses, J. I., et al. 2014a, *Icarus*, 243, 494
- Orton, G. S., Moses, J. I., Fletcher, L. N., et al. 2014b, *Icarus*, 243, 471
- Reuter, D. C., & Sirota, J. M. 1994, *Astrophys. J.*, 428, L77
- Richard, C., Gordon, I. E., Rothman, L. S., et al. 2012, *Journal of Quantitative Spectroscopy and Radiative Transfer*, 113, 1276
- Rodgers, C. D. 2000, *Inverse Methods for Atmospheric Remote Sounding: Theory and Practice (World Scientific)*
- Rothman, L. S., Gordon, I. E., Babikov, Y., et al. 2013, *J. Quant. Spectro. Rad. Trans.*, 130, 4
- Schaefer, J. 1987, *Astron. Astrophys.*, 182, L40

Schäfer, J., & Köhler, W. E. 1989, Z. Physik D, 13, 217

Trafton, L. M., Kim, S. J., Geballe, T. R., & Miller, S. 1997, Icarus, 130, 544

Stoicheff, B. P. 1957, Can. J. Phys., 35, 730

Wells, M., Pel, J.-W., Glasse, A., et al. 2015, PASP, 127, 646